

Optimal wavelength band clustering for multispectral iris recognition

Yazhuo Gong,¹ David Zhang,^{2,*} Pengfei Shi,¹ and Jingqi Yan¹

¹Institute of Image Processing & Pattern Recognition, Shanghai Jiao Tong University, Shanghai, China

²Biometrics Research Centre, Department of Computing, Hong Kong Polytechnic University, Kowloon, Hong Kong, China

*Corresponding author: csdzhang@comp.polyu.edu.hk

Received 8 December 2011; revised 19 April 2012; accepted 7 May 2012;
posted 7 May 2012 (Doc. ID 159546); published 22 June 2012

This work explores the possibility of clustering spectral wavelengths based on the maximum dissimilarity of iris textures. The eventual goal is to determine how many bands of spectral wavelengths will be enough for iris multispectral fusion and to find these bands that will provide higher performance of iris multispectral recognition. A multispectral acquisition system was first designed for imaging the iris at narrow spectral bands in the range of 420 to 940 nm. Next, a set of 60 human iris images that correspond to the right and left eyes of 30 different subjects were acquired for an analysis. Finally, we determined that 3 clusters were enough to represent the 10 feature bands of spectral wavelengths using the agglomerative clustering based on two-dimensional principal component analysis. The experimental results suggest (1) the number, center, and composition of clusters of spectral wavelengths and (2) the higher performance of iris multispectral recognition based on a three wavelengths–bands fusion. © 2012 Optical Society of America

OCIS codes: 100.2000, 100.3005, 170.2945, 230.7408.

1. Introduction

Traditionally, only a narrow band of the near-infrared (NIR) spectrum (750 to 850 nm) has been utilized for iris recognition systems since this alleviates any physical discomfort from illumination, reduces specular reflections, and increases the amount of iris texture information captured for some of the iris colors. Commercial iris recognition systems predominately operate in the NIR range of the electromagnetic spectrum. The spectrums indicate that current systems are using wavelengths that peak around 850 nm (Panasonic and Oki) with a narrow band pass. However, some systems traverse into the range of 750 nm (LG) and use multiple wavelength illumination to image the iris. The IR light is invisible to the human eye, and the intricate textural pattern represented in different colored irides

is revealed under an NIR range of illumination. The texture of the iris in IR illumination has been traditionally used as a biometric indicator [1].

However, the textural content of the iris has complex components, including numerous structures and various pigments, both fibrous and cellular, that are contained on the anterior surface, including ligaments, crypts, furrows, collarettes, moles, freckles, etc. The NIR wavelengths can penetrate melanin, showing a texture that cannot be easily observed in the visible spectrum, but the cost is substantially high. Most of the texture presented in the NIR spectrum is only generated by the iris structures, not by the pigments. The effect of melanin, the major color-inducing compound, is negligible on the NIR wavelengths in iris recognition. But melanin is always imaged in certain wavelength for extraction and classification, such as in tongue image processing [2].

The above study of melanin has inspired us to consider that the iris textures generated outside the NIR

spectrum may have more information over those that are only generated in the NIR spectrum because melanin can be present in the shorter wavelengths and becomes another major source of iris texture.

Previous research has shown that matching performance is not invariant to iris color and can be improved by imaging outside the NIR spectrum and that the physiological properties of the iris (e.g., the amount and distribution of melanin) impact the transmission, absorbance, and reflectance of different portions of the electromagnetic spectrum and the ability to image well-defined iris textures [3]. Performing multispectral fusion at the score level has been proven to be feasible [4], and the multispectral information is used to determine the authenticity of the imaged iris [5–7].

However, one underlying key issue needs to be addressed well before wide application of multispectral iris recognition: how many spectra are enough for discriminating different irides? Usually, more wavelength bands provide more information; thus, higher accuracy could be expected. On the other hand, more wavelength bands require a high cost on feature extraction and matching. Furthermore, because of redundancy between different spectra, more information may fail to increase the accuracy sometime. Therefore, it is necessary to determine an optimal number of wavelength bands in a multispectral iris system design. If we can cluster the spectral wavelengths based on the maximum dissimilarity of the corresponding iris texture and choose an iris image from each classification of spectral wavelength for fusion, the two conditions of fusion strategy (completeness and no redundancy) will be simultaneously met, so the best fusion result and matching performance will most likely be achieved.

In our work, we used the agglomerative clustering based on two-dimensional principal component analysis [(2D)²PCA], determined that 3 clusters are enough to represent the 10 feature bands of spectral wavelengths, and used the iris score-level fusion to further investigate the effectiveness of the proposed optimal number of wavelength bands by the one-dimensional (1D) Log-Gabor wavelet filter approach proposed by Masek and Kovesi. Up until now, there have been no public reports on this topic for biometric research.

The remainder of this paper is organized as follows. An image acquisition system is presented in Section 2. The method for clustering wavelength bands is discussed in Section 3. The clustering results are analyzed in Section 4. A recognition performance analysis based on iris score-level fusion is presented in Section 5. The conclusions are presented in Section 6.

2. Multispectral Iris Image Acquisition System

A. Overall Design

In this work, we have analyzed the feasibility of a conventional multispectral system based on a

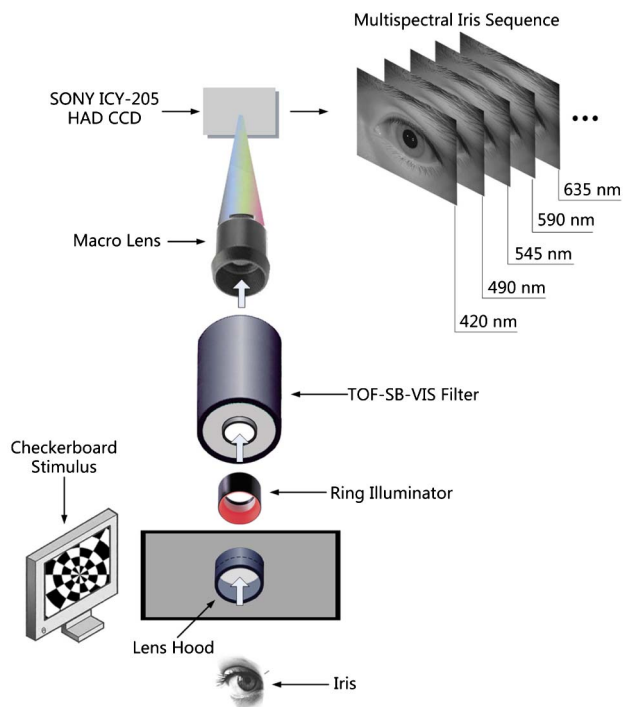


Fig. 1. (Color online) Structure of the multispectral iris acquisition system.

charge-coupled device (CCD) monochrome camera to capture iris images. One of the most challenging aspects of this research was the design of a multispectral image acquisition system.

The multispectral system developed consists of a CCD camera with a Sony ICX205 HAD CCD sensor (spectral response ranges between 400 and 1000 nm with a peak at 550 nm, 1.4 megapixels 1360 × 1024), macro manual focus (MF) lens, illumination system, and Meadowlark selectable bandwidth tunable optical filter TOF-SB-VIS (see Fig. 1).

The optical path is as follows: First, the broadband light from the illumination system is delivered to the eye, and then the reflected light from the subject's eye is collected through the center of the ring illuminator, through the band-pass filter, TOF-SB-VIS, and imaged by the ICX205 camera using a macro lens.

The camera with the Sony ICX205 HAD CCD sensor has exceptional features, including high resolution, high sensitivity, and low dark current, which are all important to multispectral imaging. The spectral response from the 400 to 1000 nm wavelength (the short wavelength IR band) is not very uniform, but we verified that the CCD response does not introduce significant errors into the experimental values after the optimization of the multispectral system.

TOF-SB-VIS is a new tunable optical filter with user-selectable bandwidths and a variable full width at half maximum available through Meadowlark Optics. By utilizing multiple liquid crystal variable retarders and polarizers, this tunable filter allows the user to switch between any wavelengths from 420 to 1100 nm. In this research, the band-pass

wavelengths of the TOF-SB-VIS were switched at 420, 490, 545, 590, 635, 665, 700, 730, 780, 810, 850 and 940 nm, which correspond to 12 kinds of narrow-band LEDs that are used in sequence to image a subject's eye across the visible and NIR bands.

The multispectral light source is a ring illuminator with six narrow wavelength-band LED lamps, is located in front of the TOF-SB-VIS (between the imaging device and the subject), and can be manually switched, allowing illumination of the captured iris with a 90 deg angle. In accordance with the spectral range of interest, narrow-band LEDs were selected at 12 wavelengths so that the corresponding band-pass wavelength outputs were delivered to the eye.

B. Data Collection

A set of 60 human irides that correspond to the right and left eyes of 30 different subjects was captured by a multispectral acquisition system. The 60 samples covered a wide range iris colorations and structures, such as rich and sparse textures.

Twenty images were taken at a specific interval of time (200 ms apart) from each the left and the right eye of a subject under 420, 490, 545, 590, 635, 665, 700, 730, 780, 810, 850 and 940 nm wavelengths, respectively. During the image capture, the subject watched the center of a ring illumination. Sample multispectral iris images that pertain to a single eye are shown in Fig. 2. We deliberately selected images whose pupil radius has a relatively consistent and small size to observe the differences in iris texture across all spectral wavelengths.

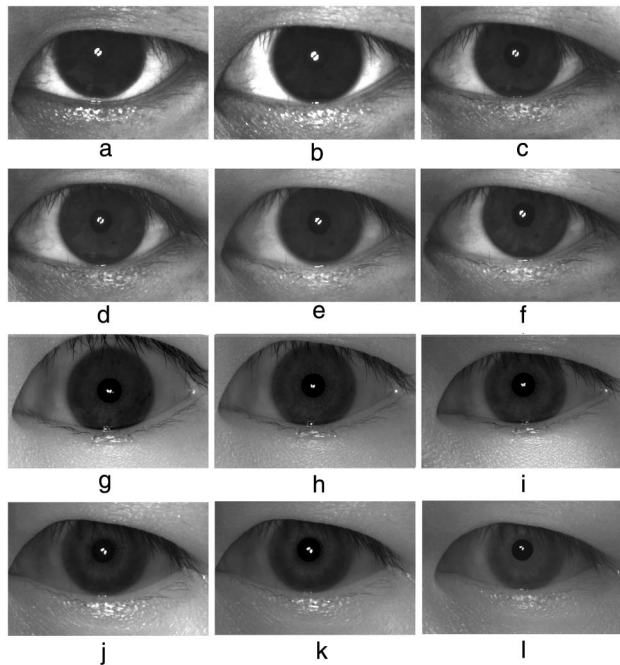


Fig. 2. Sample images obtained at wavelengths of a. 420 nm, b. 490 nm, c. 545 nm, d. 590 nm, e. 635 nm, f. 665 nm, g. 700 nm, h. 730 nm, i. 780 nm, j. 810 nm, k. 850 nm, and l. 940 nm.

3. Clustering Method of the Spectral Wavelengths

A. Data Organization of Dissimilarity Matrix

Suppose we have B bands of spectral wavelengths and S iris images from the same eye of the same subject captured under each band of spectral wavelengths, so the total number of iris images is $S \times B$. Based on the definition of the distance, we can compute the distance between any pair of images, T_i and T_j , (whether from the same or different spectral wavelengths) as the generic dissimilarity measure. We can embed the resulting dissimilarity data in matrix A ($N \times N$), and the elements of A are defined as

$$A(i,j) = d(T_i, T_j), \quad i, j = 1, \dots, N, \quad N = S \times B. \quad (1)$$

The image axis runs on the horizontal (left to right) and vertical (top to bottom) axes of A and along its main diagonal, where self-similarity is maximal. According to the order of time stamp and increasing wavelength, N iris images of the same eye can be arranged as a sequence along the axis. The iris images of the same spectral wavelength are all continuously captured, so these images will be adjacent in the axis (see Fig. 3).

The image-indexed dissimilarity matrix A can be visualized as a square image. Each pixel i, j is colored with a gray scale value proportional to the dissimilarity measure $d(T_i, T_j)$. These visualizations allowed us to clearly see the structure of a multispectral iris image sequence. Regions of the highest similarity, generated from a similar iris texture within the same spectral wavelength, appear as the brightest squares on the diagonal. The relatively brighter rectangular regions off the main diagonal indicate the similarity between the different spectral wavelengths (see Fig. 3).

B. (2D)²PCA

We then determined the specific definition of the distance measure, and discovered that the (2D)²PCA

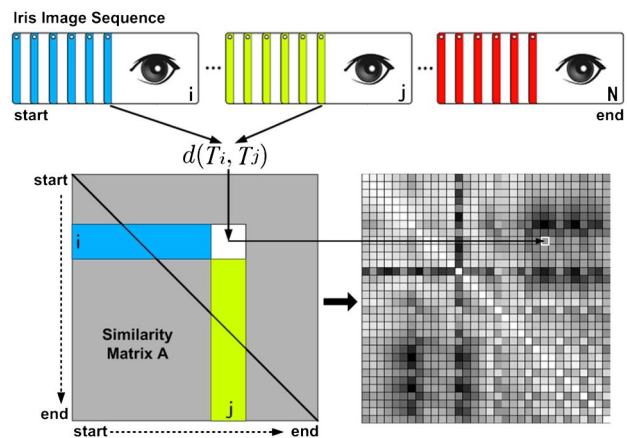


Fig. 3. (Color online) Structure of the image-indexed dissimilarity matrix A .

method [8] is a good choice for iris images. The (2D)²PCA method can alleviate the small sample size problem in a subspace analysis and preserve the image local structural information.

In this work, the (2D)²PCA analysis was simultaneously done for different bands of spectral wavelengths and yielded a joint eigenstructure across two bands of spectral wavelengths, which was used in the distance measurement between two iris images captured under different spectral wavelengths.

We denote by X_s^b , the s th iris image of the band b th, and by $X_s^{b+b'}$, the s th iris image of the union including bands b th and b' th (this union includes 2 S iris images, $X_s^{b+b'} \in \text{band } b^{\text{th}} \cup \text{band } b'^{\text{th}}$). $X_s^{b+b'}$ is an $I_r \times I_c$ matrix, where I_r and I_c represent the numbers of columns and rows of the normalized image. We used the homogenous rubber sheet model proposed by Daugman to normalize the iris image by remapping each pixel within the iris region to a pair of polar coordinates (r, θ) , where r is on the interval $[0,1]$ and θ is angle $[0,2\pi]$. For each normalized image, $I_r = 360$ and $I_c = 60$. The covariance matrices along the row and column directions of the bands b th and b' th are computed as

$$G_1^{b+b'} = \frac{1}{2S} \sum_{s=1}^{2S} (X_s^{b+b'} - \bar{X}^{b+b'})^T (X_s^{b+b'} - \bar{X}^{b+b'}),$$

$$G_2^{b+b'} = \frac{1}{2S} \sum_{s=1}^{2S} (X_s^{b+b'} - \bar{X}^{b+b'}) (X_s^{b+b'} - \bar{X}^{b+b'})^T, \quad (2)$$

where the mean vector is defined as

$$\bar{X}^{b+b'} = \frac{1}{2S} \sum_{s=1}^{2S} X_s^{b+b'}.$$

The project matrix $V_1^{b+b'} = [V_{11}^{b+b'}, V_{12}^{b+b'}, \dots, V_{1k_1^{b+b'}}^{b+b'}]$ is composed of the orthogonal eigenvectors of

$G_1^{b+b'}$, which correspond to $k_1^{b+b'}$ the largest eigenvalues, and the projection matrix $V_2^{b+b'} = [V_{21}^{b+b'}, V_{22}^{b+b'}, \dots, V_{2k_2^{b+b'}}^{b+b'}]$ consists of the orthogonal eigenvectors of $G_2^{b+b'}$, which correspond to the $k_2^{b+b'}$ largest eigenvalues. $k_1^{b+b'}$ and $k_2^{b+b'}$ can be determined by a threshold:

$$\sum_{j_c=1}^{k_1^{b+b'}} \lambda_{1j_c}^{b+b'} \left/ \sum_{j_c=1}^{I_c} \lambda_{1j_c}^{b+b'} \right. \geq C_u, \quad (3)$$

$$\sum_{j_r=1}^{k_2^{b+b'}} \lambda_{2j_r}^{b+b'} \left/ \sum_{j_r=1}^{I_r} \lambda_{2j_r}^{b+b'} \right. \geq C_u, \quad (4)$$

where $\lambda_{11}^{b+b'}, \lambda_{12}^{b+b'}, \dots, \lambda_{1I_c}^{b+b'}$ are the I_c eigenvalues of $G_1^{b+b'}$, $\lambda_{21}^{b+b'}, \lambda_{22}^{b+b'}, \dots, \lambda_{2I_r}^{b+b'}$ are the I_r eigenvalues of $G_2^{b+b'}$, and C_u is a preset threshold, $C_u = 0.5$, which determines how many of the principle eigenvalues are employed in the distance calculation.

Next, we yield the joint eigenstructure $V_1^{b+b'}$ and $V_2^{b+b'}$ across two bands of spectral wavelengths b th and b' th, and the space spanned by these eigenvectors is specified for the distance measurement of iris images from these two corresponding bands (see Fig. 4).

An image T^b of the band b th will be matched with another image $T^{b'}$ of the band b' th, and the two images T^b and $T^{b'}$ are all captured from the same eye of the same subject. These two images should be projected to \hat{T}^b and $\hat{T}^{b'}$ by $V_1^{b+b'}$ and $V_2^{b+b'}$, and the distance of T^b and $T^{b'}$ is defined as

$$d^{b+b'} = \|\hat{T}^b - \hat{T}^{b'}\|$$

$$= \|V_2^{b+b'} T^b V_1^{b+b'} - V_2^{b+b'} T^{b'} V_1^{b+b'}\|. \quad (5)$$

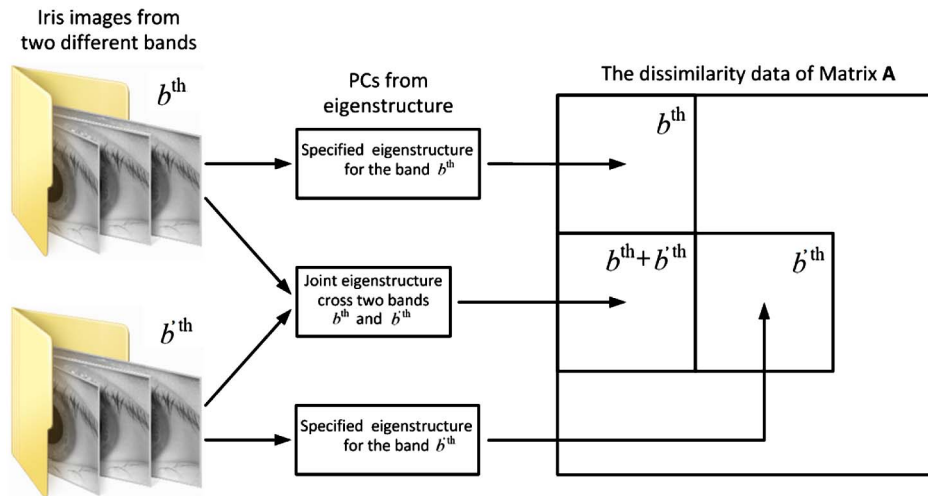


Fig. 4. (Color online) Two types of principle components generated from specified and joint eigenstructures and the correspondence with the dissimilarity data of matrix A.

In terms of the distance of the two images within band b th, the above algorithm will be slightly simplified. The covariance matrices along the row and column directions of band b th are computed as

$$G_1^b = \frac{1}{S} \sum_{s=1}^S (X_s^b - \bar{X}^b)^T (X_s^b - \bar{X}^b),$$

$$G_2^b = \frac{1}{S} \sum_{s=1}^S (X_s^b - \bar{X}^b) (X_s^b - \bar{X}^b)^T, \quad (6)$$

where $\bar{X}^b = \frac{1}{S} \sum_{s=1}^S X_s^b$, and other calculations are similar to the above algorithm. Finally, we get the eigenstructure V_1^b and V_2^b , which corresponds to band b th, and the space spanned by these eigenvectors is specified for the distance measurement of iris images from the same band (see Fig. 4).

C. Agglomerative Clustering

Suppose we have B bands of spectral wavelengths and K segments $\{p_1, \dots, p_K\}$ of variable lengths ($K \leq B$). Here, we define a collection of wavelengths as a “segment.” We can compute the mean vector and covariance matrices of each image based on Eq. (2) and then compute the distance of the two images based on Eq. (5).

Intersegment dissimilarity is defined as the Kullback–Leibler (KL) divergence [9] between two discrete random probability distributions with the distance statistics of the segments. For probability distributions P and Q of a discrete random variable, their K -L divergence is defined to be [10–13]

$$D_{\text{KL}}(P||Q) = \sum_i P(i) \ln \frac{P(i)}{Q(i)}. \quad (7)$$

The KL divergence is not symmetric, but a symmetric variation can be constructed from the sum of the two KL divergence as [14]

$$D_{\text{KL}}(P, Q) = \frac{1}{2} [D_{\text{KL}}(P||Q) + D_{\text{KL}}(Q||P)]. \quad (8)$$

So, the dissimilarity between segments p_i and p_j can be defined as

$$d_{\text{seg}}(p_i, p_j) = \exp(-D_{\text{KL}}(p_i, p_j)), \quad d_{\text{seg}}(p_i, p_j) \in (0, 1]. \quad (9)$$

We compute the intersegment dissimilarity between each pair of segments and embed them into a segment-indexed dissimilarity matrix $A_s(K \times K)$, analogous to the image-indexed dissimilarity matrix $A(N \times N)$, as

$$A_s(i, j) = d_{\text{seg}}(p_i, p_j), \quad i, j = 1, \dots, K. \quad (10)$$

The agglomerative algorithm [15] is used to cluster the K segments $\{p_1, \dots, p_K\}$ based on the segment-indexed dissimilarity matrix A_s . The input of agglomerative algorithm is the matrix $A_s(K \times K)$, the initial dissimilarity is the matrix $A_s^0 = A_s$. At each level t , when two segments are merged into one, the size of the dissimilarity matrix A_s^t becomes $(K - t) \times (K - t)$. A_s^t follows A_s^{t-1} by (1) deleting the two rows and columns that correspond to the merged clusters and (2) adding a new row and column that contain the distance between the newly formed cluster and the old (unaffected at this level) cluster. The distance between the newly formed cluster C_q (the result of merging C_i and C_j) and an old cluster C_s is defined as the KL distance (see Fig. 5).

The agglomerative clustering algorithm is as follows:

1. Initialization:
 - 1.1 The initial segments ψ_0 for the agglomerative algorithms consist of K segments: $\psi_0 = \{\{P_i\}, i = 1, 2, \dots, K\}$.
 - 1.2 The initial dissimilarity matrix $A_s^0 = A_s$.
 - 1.3 The level of agglomerative algorithm $t = 0$.
2. Repeat:
 - 2.1 $t = t + 1$.
 - 2.2 Find C_i and C_j such that $d_{\text{KL}}(C_i, C_j) = \min_{r, s=1, \dots, K, r \neq s} d_{\text{KL}}(C_r, C_s)$.
 - 2.3 Merge C_i and C_j into a single cluster C_q and form $\psi_t = (\psi_{t-1} - \{C_i, C_j\}) \cup \{C_q\}$.
 - 2.4 Define the dissimilarity matrix A_s^t from two matrices, A_s^{t-1} and A , as previously explained in the text and shown in Fig. 5.

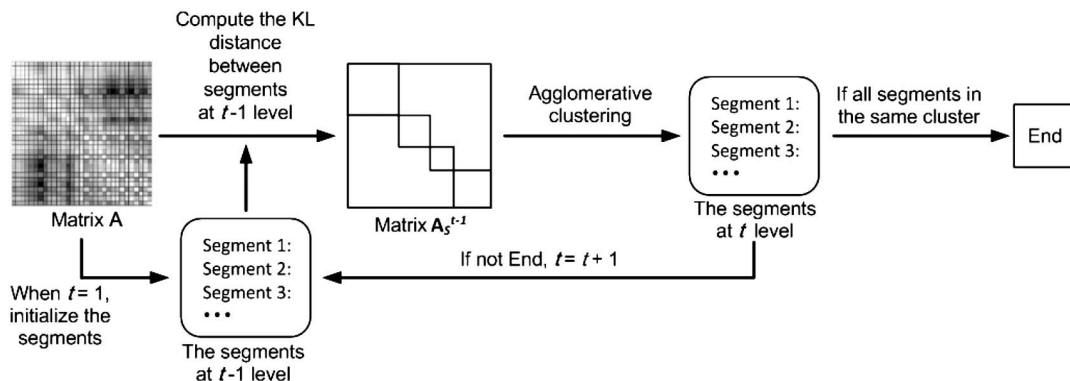


Fig. 5. Diagram of agglomerative clustering.

- Repeat until ψ_{K-1} clustering is formed; that is, all segments in the same cluster.

By applying the above process, we can get the clustering hierarchy and then determine the number of clusters by analyzing the lifetime of the hierarchy. A diagram of the proposed method is shown in Fig. 6.

4. Experimental Results

A. Iris Database

A dataset that contained samples from 60 irides was used to conduct the following study. Our iris database, which uses the proposed multispectral iris acquisition system, was created with 30 subjects. In this database, 25 were male. Twenty images, which were taken from each the left and right eye of a subject, were selected under 12 spectral bands that corresponded to 420, 490, 545, 590, 635 nm, 665, 700, 730, 780, 810, 850, and 940 nm, respectively. In total, we collected 14,400 iris images for this database. The image resolution was 640×480 .

In this work, we used Daugman's rubber sheet model [16] to get the normalized iris images. After normalization, only 10 spectral bands longer than 500 nm were used in the experiment, since in the 420 and 490 nm images, the gray scales of the pupil and iris were too close to be correctly segmented and the iris textural clarity was too low to benefit this study.

2. Results of the Proposed Method

The distance based on (2D)²PCA is relatively sensitive to pupil dilation, so we used six images with the smallest pupil of each spectral band, and, in total, 3,600 iris images were used for this experiment. The radius of the pupils in these images was very small and changed only in a limited range of size. In consideration of the degree of iris deformation, we used the ratio of pupil radius to iris radius as $T = R_p/R_i$ to measure the influence of pupillary constriction. In this work, the T of all 3,600 images was in the range of 0.23 to 0.35.

For each iris, the image-indexed dissimilarity matrix $A(60 \times 60)$ is shown in Fig. 7. Regions of the highest similarity, generated from similar iris texture within the same spectral wavelength, appeared

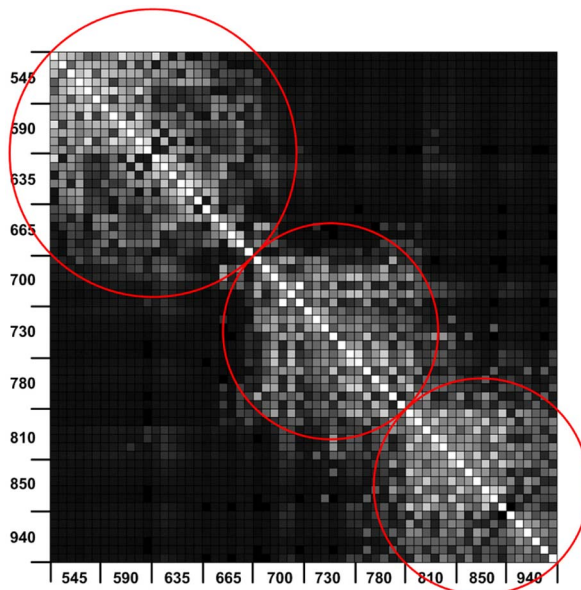


Fig. 7. (Color online) Image-indexed dissimilarity matrix A.

as the brightest squares on the diagonal. The relatively brighter rectangular regions off the main diagonal indicated the similarity between the different spectral wavelengths, as shown in Fig. 7.

We considered these 10 wavelengths as the input of the clustering algorithm, computed the intersegment dissimilarity (the KL distance) between each pair of segments, embedded them into the first segment-indexed dissimilarity matrix $A_s^0(10 \times 10)$, and used an agglomerative clustering algorithm to merge clusters for the first time. Then, we repeat the above process, and got the dendrogram from the clustering hierarchy (see Fig. 8).

As explained earlier, this algorithm determined a whole hierarchy of spectral wavelength clustering, rather than a single clustering. However, in this work, we were only interested in the specific clustering that best fit the data. Thus, we had to decide which clustering of the produced hierarchy was most suitable for the data. Equivalently, we had to determine the appropriate level to cut the dendrogram that corresponded to the clustering hierarchy.

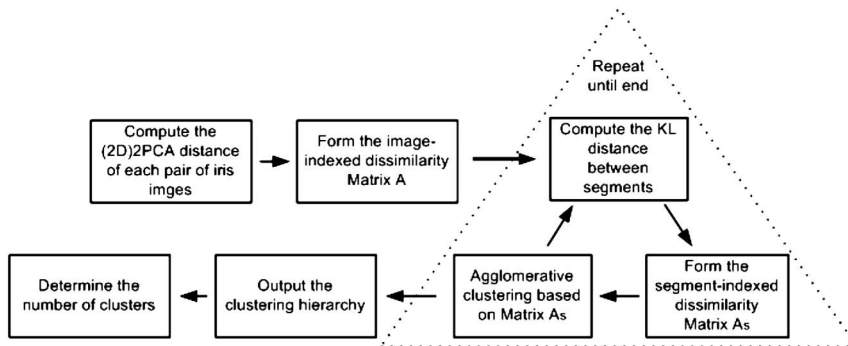


Fig. 6. Diagram of the proposed method.

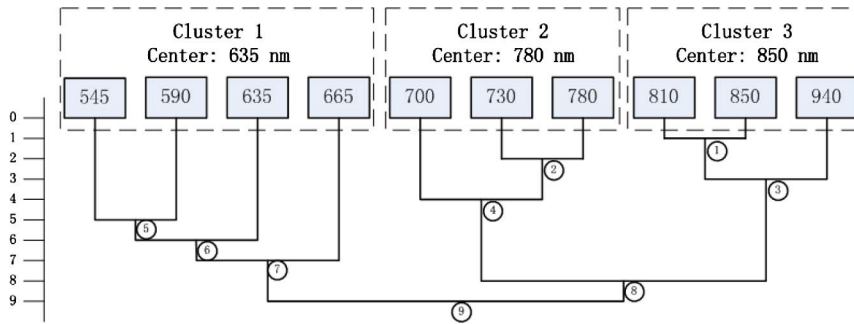


Fig. 8. (Color online) Dendrogram from the clustering hierarchy.

First, the best clustering within a given hierarchy generated by an agglomerative algorithm needed to be determined. Clearly, this was equivalent to the identification of the number of clusters that best fit the data. An intuitive approach was to search in the dendrogram for clusters that had a large lifetime, which is generally used as the criteria for cluster validity of the proposed method. The lifetime of a cluster was defined as the absolute value of the difference between the level at which it is created and the level at which it is absorbed into a large cluster [17,18]. As shown in Fig. 8, Cluster 3 was created at level 3 and absorbed into a large cluster at level 8, so the absolute value of the difference between these two levels was 5, which is the largest lifetime of all. According to the lifetime principle, the dendrogram in Fig. 8 suggests that 3 major clusters best fits all 10 multispectral bands. The clustering result of these three clusters is listed in Table 1.

The distance map between different wavelengths is plotted in Fig. 7. As can be seen from Fig. 7, there are roughly three bright blocks. We can find the physical explanation for the clustering result. According to the spectrum definition, the spectral wavelengths longer than 800 nm can be seen as the typical NIR spectrum, and ones that are shorter than 700 nm are considered as visible light. The wavelengths from 700 to 800 nm are the transitional area between visible light and NIR, which is near the upper limit for response by a typical human eye. The above division of wavelengths is consistent with the clustering result.

Second, we found the cluster centers by using the dissimilarity data in matrix \mathbf{A} to calculate the center of the corresponding cluster. Suppose we have \mathbf{B} bands of spectral wavelengths and S iris images from same subject captured under each band of spectral wavelengths. We denote by X_s^b , the s th iris image under the b th band. The distance $d_{\text{cross}}(b, b')$ between bands b th and b' th is defined as

$$d_{\text{cross}}(b, b') = \sum_{p=1}^S \sum_{q=1}^S d^{b+b'}(X_p^b, X_q^{b'}), \quad (11)$$

and $d^{b+b'}$ is defined in Section 3, whose value is the elements of matrix \mathbf{A} . For a given band b th, we can calculate the average distance between b th and other bands in the same cluster as

$$d_{\text{ave}}(b) = \frac{1}{N-1} \sum_{n=1}^{N-1} d_{\text{cross}}(b, n). \quad (12)$$

N is the number of spectral bands within this cluster, so the center of cluster is

$$C = \{i | \arg \min d_{\text{ave}}(i)\}, \quad i = 1, 2, \dots, N. \quad (13)$$

Using this method, we were able to determine the three corresponding cluster centers.

Note that in each run of the proposed method, the clustering results were based on the dataset that contained 60 images captured from one specific iris, so we repeated the proposed method on the image dataset. The most frequent cluster number and centers were kept as the final result because there was the possibility that the clustering results were influenced by the images of a special iris and the different choice of parameter values.

After testing all 3,600 images from 60 irides, the final clustering hierarchy was the same as Table 1, and the three corresponding cluster centers were as follows: The Cluster 1 center was 635 nm, the Cluster 2 center was 780 nm, and the Cluster 3 center was 850 nm.

5. Performance Analysis

To demonstrate whether there is the optimal number of wavelength bands for multispectral fusion, the verification experiment based on the performance of iris recognition was implemented on our iris image database. In the verification experiment, we used Masek and Kovess's [19] 1-D Log-Gabor wavelet method, which is the most popular comparison method in the literature due to the accessibility of their source code.

Table 1. Clustering Result of Three Clusters

Cluster	Wavelengths
1	545 nm, 590 nm, 635 nm, 665 nm
2	700 nm, 730 nm, 780 nm
3	810 nm, 850 nm, 940 nm

Ten spectral bands longer than 500 nm were used in this experiment, since the textural clarity of the images under 420 and 490 nm was too low to benefit this study. So, we selected 10 images corresponding to each eye under each spectral band, a total of 6,000 out of 14,400 iris images, for the recognition experiment. There were two kinds of matching scores used—intraspectral genuine scores and intraspectral impostor scores. Intraspectral genuine scores are calculated from two iris images of the same eye under the same wavelength. Intraspectral impostor scores are calculated from two images—one of a certain left eye and the other of a different left eye (that is, both from the eye on the same side) and captured under the same wavelength. A total of 27,000 intraspectral genuine scores and 870,000 intra-spectral impostor scores were generated.

To find the optimal combination for a given number of wavelength clusters, many algorithms could be used, such as divergence [20], mutual information [21], and entropy [22]. Here, an exhaustive search was implemented as it decreased the possibility of missing any optimal combinations. We computed the equal error rate (EER, where the false rejection rate is equal to the false acceptance rate) corresponding to each combination for a given number of wavelength clusters and selected the lowest one. For example, the EER under one spectral wavelength is shown in Fig. 9, which is the recognition performance without any multispectral fusion, and the lowest one is under 700 nm.

Generally, more texture information across different wavelengths is used, and better recognition performance can be achieved. However, since there is some possible overlapping of the discriminating information between different wavelengths, a simple sum of the matching scores of all wavelengths may not improve the final accuracy. The overlapping part between the two iris code bit vectors under two different wavelengths would be counted twice by using the sum score-level fusion [23], which is the most popular of the fusion techniques, on the dataset. Such kind of overcomputing may make the simple score-level fusion fail.

When a score-level fusion strategy can reduce the overlapping effect, better verification results can be

expected. In combinatorics, the inclusion–exclusion principle [24] (which is attributed to Abraham de Moivre) is an equation relating the sizes of two sets and their union. It states that if A and B are two (finite) sets, let $|A|$ denote the cardinality of set A , and it then follows immediately that

$$|A \cup B| = |A| + |B| - |A \cap B|, \quad (14)$$

where \cup denotes union and \cap denotes intersection. The meaning of the statement is that the number of elements in the union of the two sets is the sum of the elements in each set, respectively, minus the number of elements that are in both. More generally, for finite sets A_1, \dots, A_n , one has the identity as follows:

$$\begin{aligned} \left| \bigcup_{i=1}^n A_i \right| &= \sum_{i=1}^n |A_i| - \sum_{i,j:1 \leq i < j \leq n} |A_i \cap A_j| \\ &+ \sum_{i,j,k:1 \leq i < j < k \leq n} |A_i \cap A_j \cap A_k| - \dots \\ &+ (-1)^{n-1} |A_1 \cap \dots \cap A_n|. \end{aligned} \quad (15)$$

Under wavelength i , based on two iris code bit vectors are denoted as $\{\text{code}_{A,i}, \text{code}_{B,i}\}$, and mask bit vectors denoted as $\{\text{mask}_{A,i}, \text{mask}_{B,i}\}$, we can compute the raw Hamming distance as follows:

$$\begin{aligned} HD_{\text{raw},i}(A, B) &= \frac{\|(\text{code}_{A,i} \otimes \text{code}_{B,i}) \cap \text{mask}_{A,i} \cap \text{mask}_{B,i}\|}{\|\text{mask}_{A,i} \cap \text{mask}_{B,i}\|}. \end{aligned} \quad (16)$$

So, based on Eqs. (14) to (16), a score-level fusion rule is defined that tends to minimize the overlapping effect on the fused score as follows:

$$\begin{aligned} HD_{\text{sum}(1,2)}(A, B) &= HD_{\text{raw},1}(A, B) + HD_{\text{raw},2}(A, B) \\ &- \frac{HD_{\text{raw},1}(A, B) + HD_{\text{raw},2}(A, B)}{2} \\ &\times P_{1,2}(A, B), \end{aligned} \quad (17)$$

where $P_{1,2}(A, B)$ is the overlapping percentage between two iris code bit vectors exacted from the

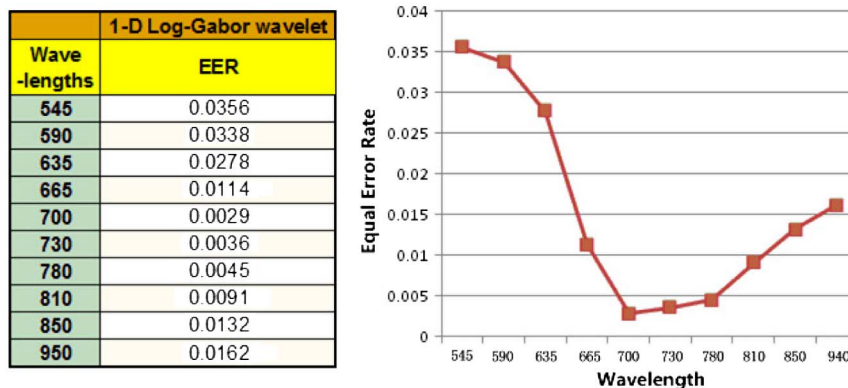


Fig. 9. (Color online) Wavelength versus EER.

same iris but captured under two different bands of wavelength, defined as follows:

$$P_{1,2}(A,B) = 1 - \left(\frac{\|(\text{code}_{A,1} \otimes \text{code}_{A,2}) \cap \text{mask}_{A,1} \cap \text{mask}_{A,2}\|}{\|\text{mask}_{A,1} \cap \text{mask}_{A,2}\|} + \frac{\|(\text{code}_{B,1} \otimes \text{code}_{B,2}) \cap \text{mask}_{B,1} \cap \text{mask}_{B,2}\|}{\|\text{mask}_{B,1} \cap \text{mask}_{B,2}\|} \right) \times \frac{1}{2} \quad (18)$$

Similarly, we can extend the multispectral score fusion scheme to fuse more bands of wavelength, such as the three spectral bands as in Eq. (19):

$$\begin{aligned} \text{HD}_{\text{sum}(1,2,3)}(A,B) &= \text{HD}_{\text{raw},1}(A,B) + \text{HD}_{\text{raw},2}(A,B) + \text{HD}_{\text{raw},3}(A,B) \\ &\quad - \frac{\text{HD}_{\text{raw},1}(A,B) + \text{HD}_{\text{raw},2}(A,B)}{2} \times P_{1,2}(A,B) \\ &\quad - \frac{\text{HD}_{\text{raw},1}(A,B) + \text{HD}_{\text{raw},3}(A,B)}{2} \times P_{1,3}(A,B) \\ &\quad - \frac{\text{HD}_{\text{raw},2}(A,B) + \text{HD}_{\text{raw},3}(A,B)}{2} \times P_{2,3}(A,B) \\ &\quad - \frac{\text{HD}_{\text{raw},1}(A,B) + \text{HD}_{\text{raw},2}(A,B) + \text{HD}_{\text{raw},3}(A,B)}{2} \\ &\quad \times P_{1,2,3}(A,B). \end{aligned} \quad (19)$$

Using the proposed score-level fusion strategy, we obtained the lowest EER for each combination, which are listed in Table 2.

Table 2 shows more wavelength bands for fusion and higher accuracy of recognition. For example, the fusion of two bands could reduce the EER from 0.00292 to 0.00161, and the fusion of three bands could reduce the EER from 0.00161 to 0.00119. However, the improvement from three bands to four bands is very small at only 0.00001. Using statistical analysis [25], the difference between the fusion of four bands and three bands is not statistically significant. All ten wavelength bands for fusion could achieve the smallest EER, 0.00117, and there is very little improvement from the fusion of three bands. This finding is consistent with the finding in the wavelength clustering—three clusters are enough to represent the ten wavelengths, and score-level fusion based on three clusters can obtain almost the best performance in multispectral iris recognition.

Table 2. Fusion Result for Different Numbers of Wavelength Clusters

Number of Clusters	Optimal Combination	EER (Mean)
1	700 nm,	0.00292
2	700 nm, 850 nm	0.00161
3	665 nm, 730 nm, 850 nm	0.00119
4	665 nm, 730 nm, 810 nm, 940 nm	0.00118
10	All wavelength bands	0.00117

6. Conclusions

This work explored the possibility of clustering spectral wavelengths based on the maximum dissimilarity of iris textures. The overall goal was to determine how many bands of spectral wavelengths are enough for iris multispectral fusion and to find these bands that would provide higher performance of iris multispectral recognition.

Such an analysis is required to understand the texture from the structure and melanin of the iris that is revealed across all wavelengths from 400 to 1000 nm. So, an acquisition system has been designed to acquire a small dataset of iris images in the 420 to 940 nm wavelength range. The agglomerative clustering based on (2D)²PCA has been proposed to cluster multispectral iris images. The clustering result could be used to determine an optimal number of wavelength bands for fusion.

The clustering result shows that three wavelength bands may be enough to represent the iris features. Based on score-level fusion and exhaustive searching on all fusion candidates, three wavelength bands could get much better results than two bands and comparable results with four bands and all ten bands. This finding validates the effectiveness of the proposed clustering algorithm, and it is empirically demonstrated that three feature bands is a good option for real multispectral iris applications. The finding will be applied to the design of our future multispectral iris system. The multispectral iris images database is currently limited by the inclusion of only East Asians, so whether the finding is applicable to other groups needs further investigation.

In the future, a fusion at the image and feature levels should be investigated based on the iris images that are simultaneously acquired, and this has attracted the attention of some researchers [26–31]. More effective enhancement techniques for image quality may be explored to improve the performance of multispectral iris recognition in large datasets [32].

This work was supported by the NSFC Overseas Fund (61020106004), the China National 973 Project (2011CB302203), the GRF fund from the Hong Kong S.A.R. government, and the central fund from Hong Kong Polytechnic University.

References

1. C. K. Boyce, "Multispectral iris recognition analysis: techniques and evaluation," Master's thesis (West Virginia University, 2006), pp. 101–102.
2. Z. Liu, J.-Q. Yan, D. Zhang, and Q.-L. Li, "Automated tongue segmentation in hyperspectral images for medicine," *Appl. Opt.* **46**, 8328–8334 (2007).
3. C. L. Wilkerson, N. A. Syed, M. R. Fisher, N. L. Robinson, I. H. L. Wallow, and D. M. Albert, "Melanocytes and iris color: light-microscopic findings," *Arch. Ophthalmol.* **114**, 437–442 (1996).
4. A. Ross, R. Pasula, and L. Hornak, "Exploring multispectral iris recognition beyond 900 nm," in *Proceedings of the IEEE Third International Conference on Biometrics: Theory, Applications, and Systems, 2009* (IEEE, 2009), pp. 1–8.
5. J. Park and M. Kang, "Multispectral iris authentication system against counterfeit attack using gradient-based image fusion," *Opt. Eng.* **46**, 117003 (2007).

6. M. J. Burge and M. K. Monaco, "Multispectral iris fusion for enhancement, interoperability, and cross wavelength matching," *Proc. SPIE* **7334**, 73341D (2009).
7. L. Franssen, J. E. Coppens, and T. J. T. P. van den Berg, "Grading of iris color with an extended photographic reference set," *J. Opt.* **1**, 36–40 (2008).
8. W. Zuo, D. Zhang, and K. Wang, "Bidirectional PCA with assembled matrix distance metric for image recognition," *IEEE Trans. Syst. Man Cybern. B* **36**, 863–872 (2006).
9. T. Cover and J. Thomas, *Elements of Information Theory* (Wiley, 1991).
10. S. Ghosal, J. K. Ghosh, and R. V. Ramamoorthi, "Posterior consistency of Dirichlet mixtures in density estimation," *Ann. Stat.* **27**, 143–158 (1999).
11. S. Ghosal and A. W. van der Vaart, "Entropies and rates of convergence for maximum likelihood and Bayes estimation for mixtures of normal densities," *Ann. Stat.* **29**, 1233–1263 (2001).
12. S. Ghosal and A. W. van der Vaart, "Posterior convergence rates of Dirichlet mixtures at smooth densities," *Ann. Stat.* **35**, 697–723 (2007).
13. S. T. Tokdar, "Posterior consistency of Dirichlet location-scale mixture of normals in density estimation and regression," *Sankhya* **68**, 90–110 (2006).
14. D. H. Johnson and S. Sinanović, "Symmetrizing the Kullback–Leibler distance," in *Proceedings of IEEE Transactions on Information Theory* (IEEE, 2001), pp. 1–10.
15. K. Ozawa, "CLASSIC: a hierarchical clustering algorithm based on asymmetric similarities," *Pattern Recogn.* **16**, 201–211 (1983).
16. J. Daugman, "New methods in iris recognition," *IEEE Trans. Syst. Man Cybern. B* **37**, 1167–1175 (IEEE, 2007).
17. S. Theodoridis and K. Koutroumbas, *Pattern Recognition*, 3rd ed. (Elsevier, 2006).
18. B. Everitt, S. Landau, and M. Leese, *Cluster Analysis*, 4th ed. (Edward Arnold, 2001).
19. L. Masek, "Recognition of human iris patterns for biometric identification," M.S. thesis (University of Western Australia, 2003).
20. H. Chang, Y. Yao, A. Koschan, B. Abidi, and M. Abidi, "Spectral range selection for face recognition under various illuminations," in *Proceedings of the 15th IEEE International Conference on Image Processing* (IEEE, 2008), pp. 2756–2759.
21. B. Guo, S. R. Gunn, R. I. Damper, and J. D. B. Nelson, "Band selection for hyperspectral image classification using mutual information," *IEEE Geosci. Remote Sens. Lett.* **3**, 522–526 (2006).
22. H. Wang and E. Angelopoulou, "Sensor band selection for multispectral imaging via average normalized information," *J. Real-Time Image Proc.* **1**, 109–121 (2006).
23. A. A. Ross, K. Nadakumar, and A. K. Jain, *Handbook of Multibiometrics* (Springer, 2006).
24. L. Comtet, *Advanced Combinatorics: The Art of Finite and Infinite Expansions*, rev. enl. ed. (Reidel, 1974), pp. 176–177.
25. W. Mendenhall, R. J. Beaver, and B. M. Beaver, *Probability and Statistics* (Brooks/Cole, 2003).
26. M. Vilaseca, R. Mercadal, J. Pujol, M. Arjona, M. de Lasarte, R. Huertas, M. Melgosa, and F. H. Imai, "Characterization of the human iris spectral reflectance with a multispectral imaging system," *Appl. Opt.* **47**, 5622–5630 (2008).
27. M. Vilaseca, J. Pujol, M. Arjona, and M. de Lasarte, "Multispectral system for reflectance reconstruction in the near infrared region," *Appl. Opt.* **45**, 4241–4253 (2006).
28. Z. Guo, L. Zhang, and D. Zhang, "Feature band selection for multispectral palmprint recognition," in *Proceedings of the 20th International Conference on Pattern Recognition* (IEEE, 2010), pp. 1136–1139.
29. Z. Guo, D. Zhang, L. Zhang, W. Zuo, and G. Lu, "Empirical study of light source selection for palmprint recognition," *Pattern Recogn. Lett.* **32**, 120–126 (2011).
30. H. Wang and E. Angelopoulou, "Sensor band selection for multispectral imaging via average normalized information," *J. Real-Time Image Process.* **1**, 109–121 (2006).
31. J. C. Price, "Band selection procedure for multispectral scanners," *Appl. Opt.* **33**, 3281–3288 (1994).
32. M. Vatsa, R. Singh, and A. Noore, "Improving iris recognition performance using segmentation, quality enhancement, match score fusion and indexing," *Proc. IEEE Trans. Syst. Man Cybern. B* **38**, 1021–1035 (2008).